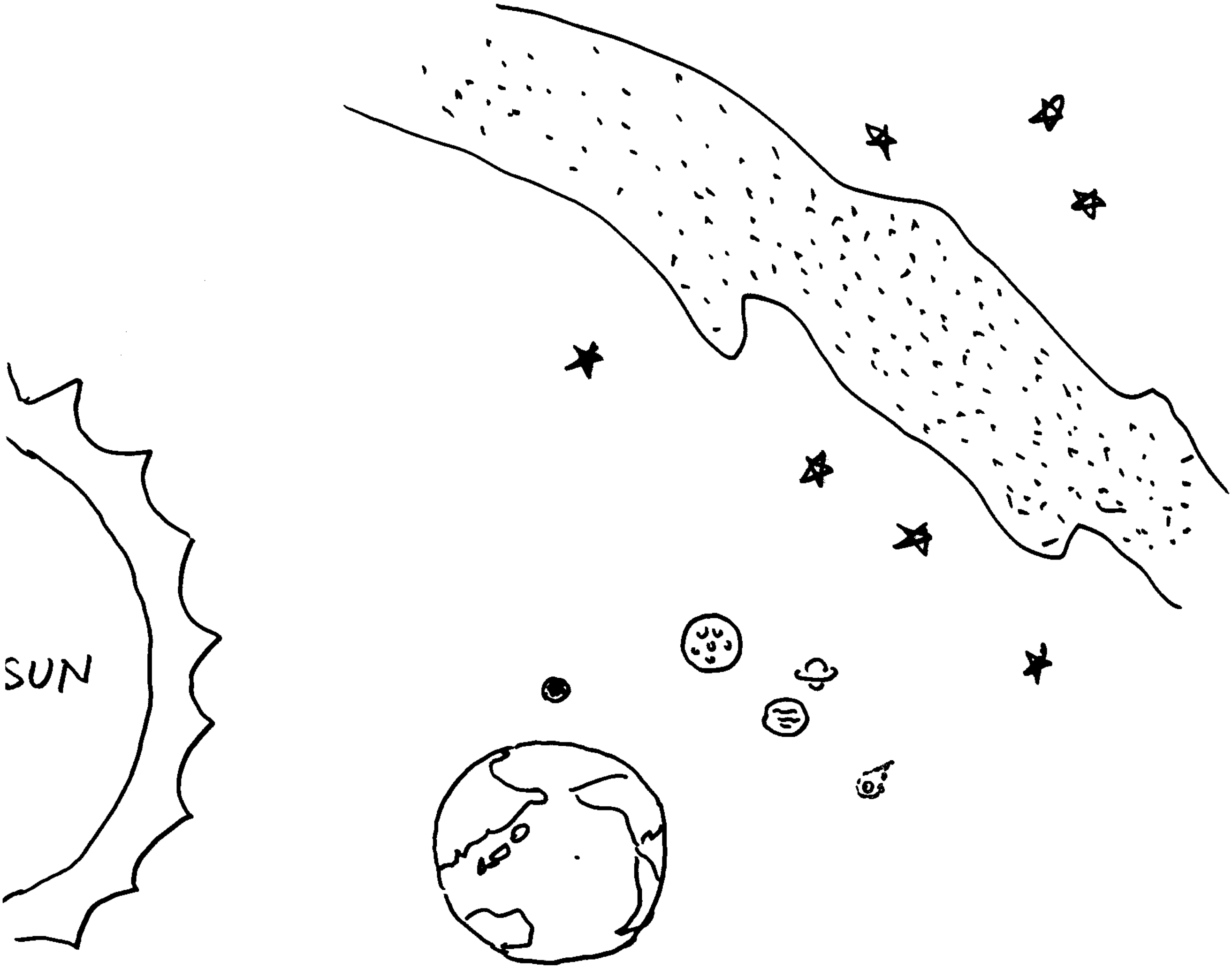

天文 & 地惑
合同セミナー

1993年 7月22、23日
東京大学理学部 3号館

地球における様々な
タイムスケール

自由落下 $\sqrt{\frac{R^3}{GM}} \sim 8\times10^{2}$ sec

振動 $\frac{2R}{v_p} \sim 1.2\times10^{3}$ sec

$\frac{2L_M}{v_s} \sim 1.0\times10^{3}$ sec

回転 $\frac{1}{\Omega} \sim 8.6\times10^{4}$ sec

……

対流 $\frac{L_c}{v_c} \sim 3\times10^{9}$ sec (外核)

$\frac{L_M}{v_M} \sim 9\times10^{14}$ sec (マントル)

熱拡散 $\frac{L_c^2}{\kappa_c} \sim 10^{18}$ sec $\Big(\frac{L_c^2}{\eta_m} \sim 2\times10^{12}$

磁気拡散

$\frac{L_M^2}{\kappa_M} \sim 10^{19}$ sec

運動量〃 $\frac{L_c^2}{\nu_c} \sim 4\times10^{19}$ sec

$\frac{L_M^2}{\nu_M} \sim 5\times10^{-5}$ sec

……

内核振動 $\sqrt{\frac{2\pi}{G\Delta\rho}} \sim 10^{4}$ sec

地球の構造とダイナミックス

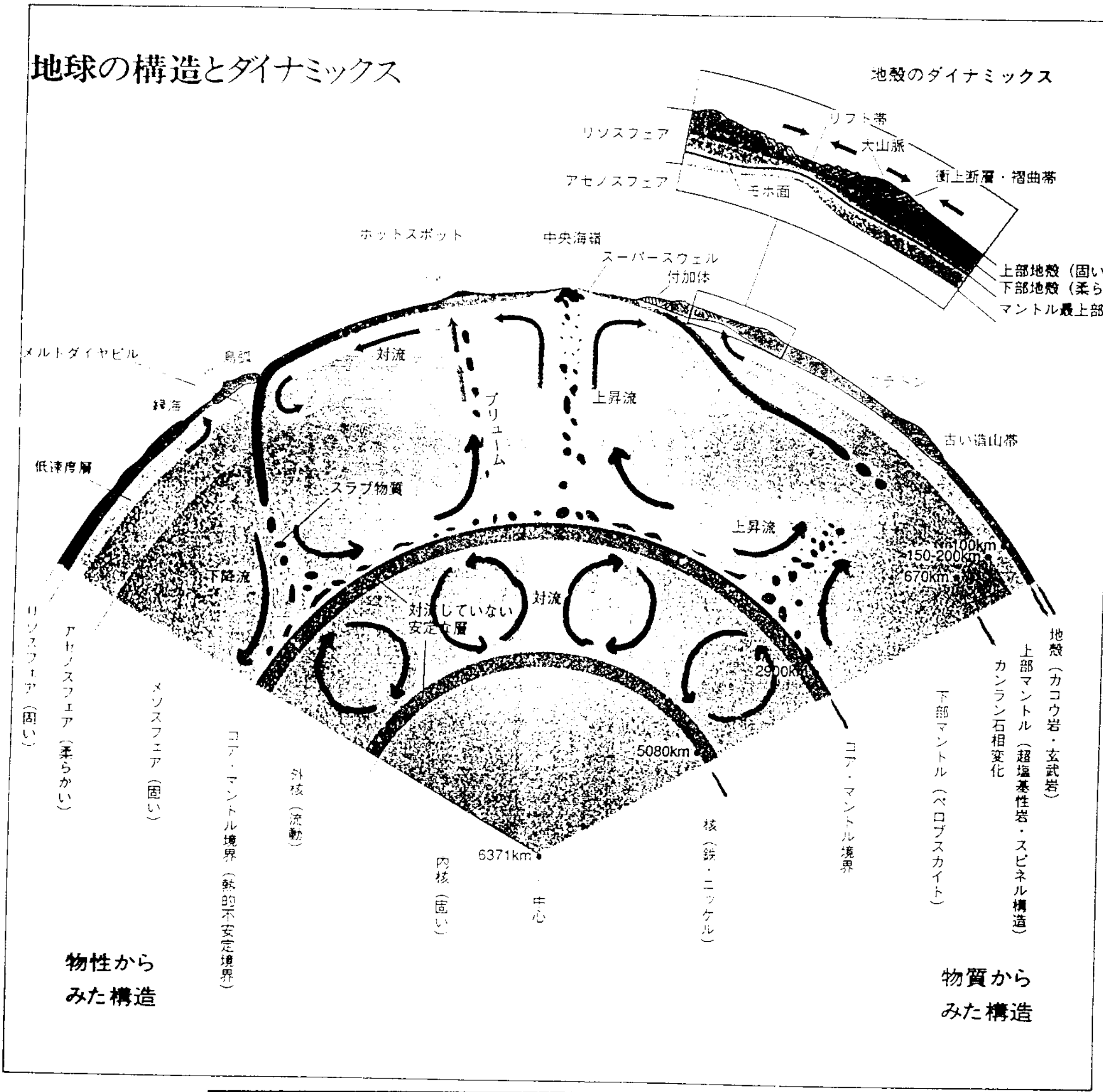
地殻のダイナミックス
リフト帯
リソスフェア
大山脈
衝上断層・褶曲帯
アセノスフェア
モホ面
上部地殻（固い
下部地殻（柔ら
マントル最上部
ホットスポット
中央海嶺
スーパースウェル
付加体
メルトダイヤピル
島弧
対流
縁海
プリューム
上昇流
テラン
古い造山帯
低速度層
スラブ物質
上昇流
100km
150-200km
670km
下降流
対流していない
安定な層
対流
2900km
5080km
6371km
リソスフェア（固い）
アセノスフェア（柔らかい）
メソスフェア（固い）
コア・マントル境界（熱的不安定境界）
外核（流動）
内核（固い）
中心
核（鉄・ニッケル）
コア・マントル境界
下部マントル（ペロブスカイト）
カンラン石相変化
上部マントル（超塩基性岩・スピネル構造）
地殻（カコウ岩・玄武岩）
物性から
みた構造
物質から
みた構造

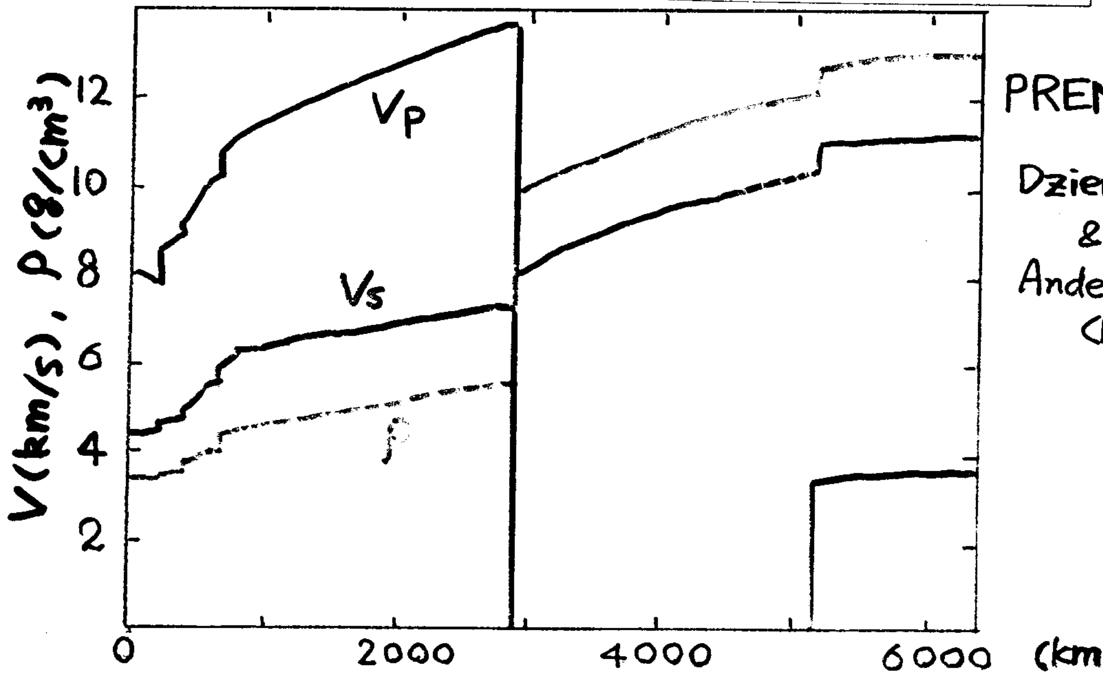

Phase の 命名

いろいろな実体波

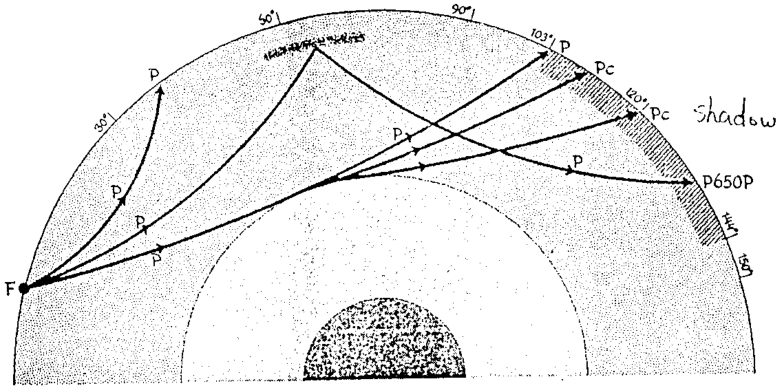
30°
50°
90°
103° P
Pc
120° Pc
P650P
144°
150°
F
P
P
P
P
P
P
P

shadow zone.

$$\begin{cases} v_p^2 = \dfrac{K + \frac{4}{3}\mu}{\rho} \\ v_s^2 = \dfrac{\mu}{\rho} \end{cases}$$

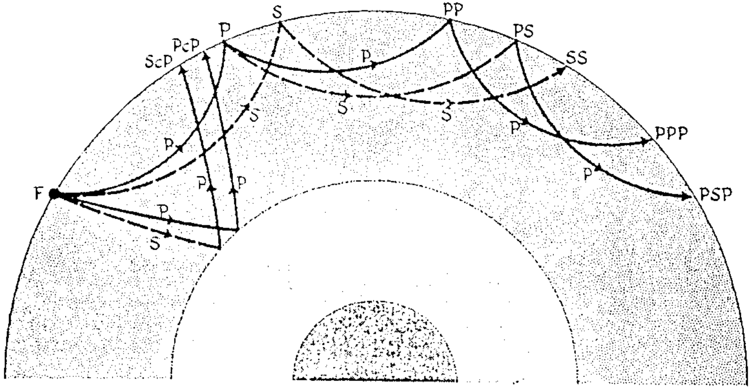
F
ScP
PcP
P
S
PP
PS
SS
PPP
PSP
P
P
P
P
S
S
S
S
P
P
P

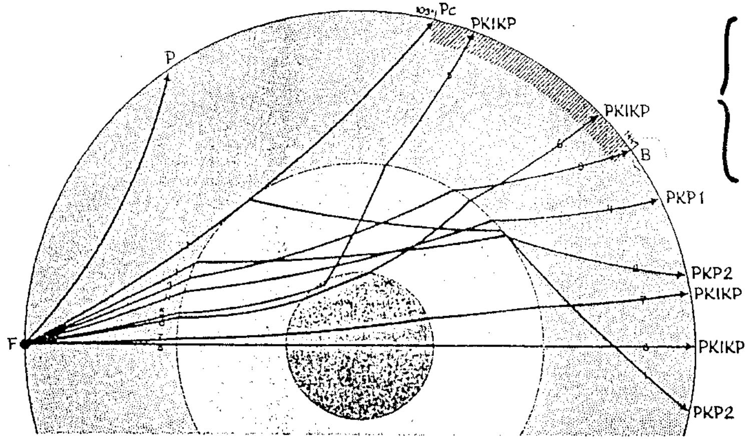
F
P
103° Pc
PKIKP
PKIKP
143
B
PKP1
PKP2
PKIKP
PKIKP
PKP2

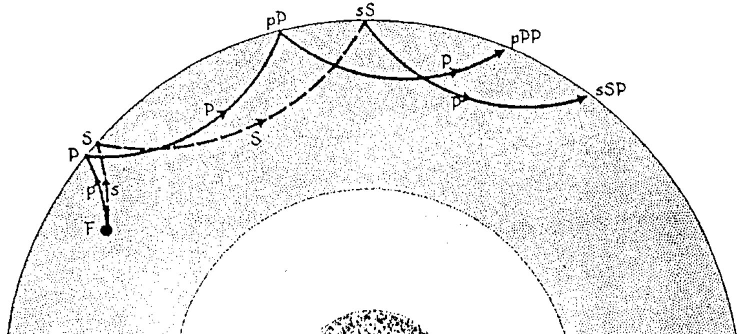
F
p
s
P
S
pP
sS
pPP
sSP
P
S
P
P

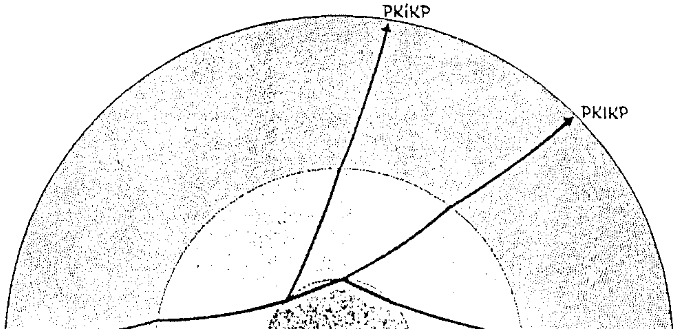
PKiKP
PKIKP

地震波形（上下動成分）

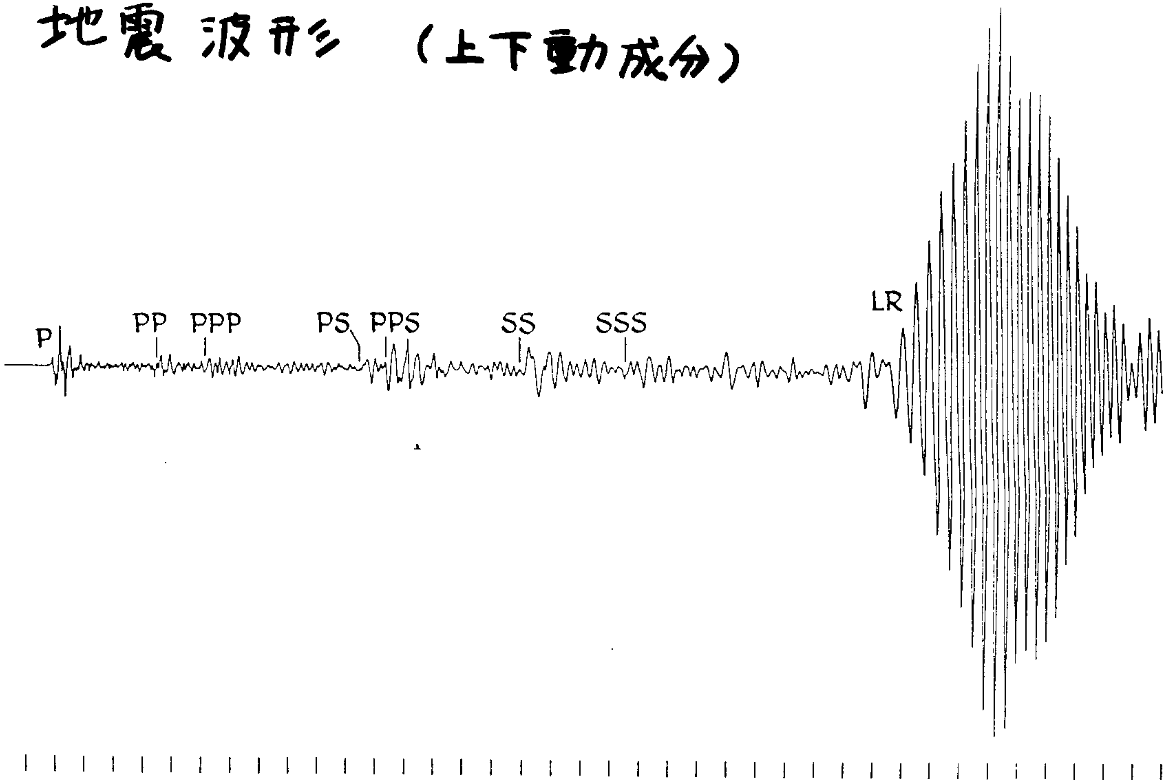

Plate 50. The Costa Rica earthquake of April 3, 1983 (M=7.2), recorded by a vertical-component broad-band system at GRF, Bayern, FRG. The distance is 86° and the focal depth is 44 km. There is 1 minute between successive time marks at the bottom of the plate. The *P* and four associated phases that have been once or twice reflected from the Earth's surface are clearly visible in the trace. Two additional surface reflections belonging to the *S*-wave group can also be identified. The complete record is, however, dominated by a fundamental-mode Rayleigh wave, developed along a mainly oceanic propagation path. The *LR* wave has a long duration and a regular dispersion, within the period interval from about 30 to 15 s, manifested by a frequency modulated quasi-sinusoidal (sweeping period) trace form. The displayed seismogram shows the ground displacement.

走時曲線

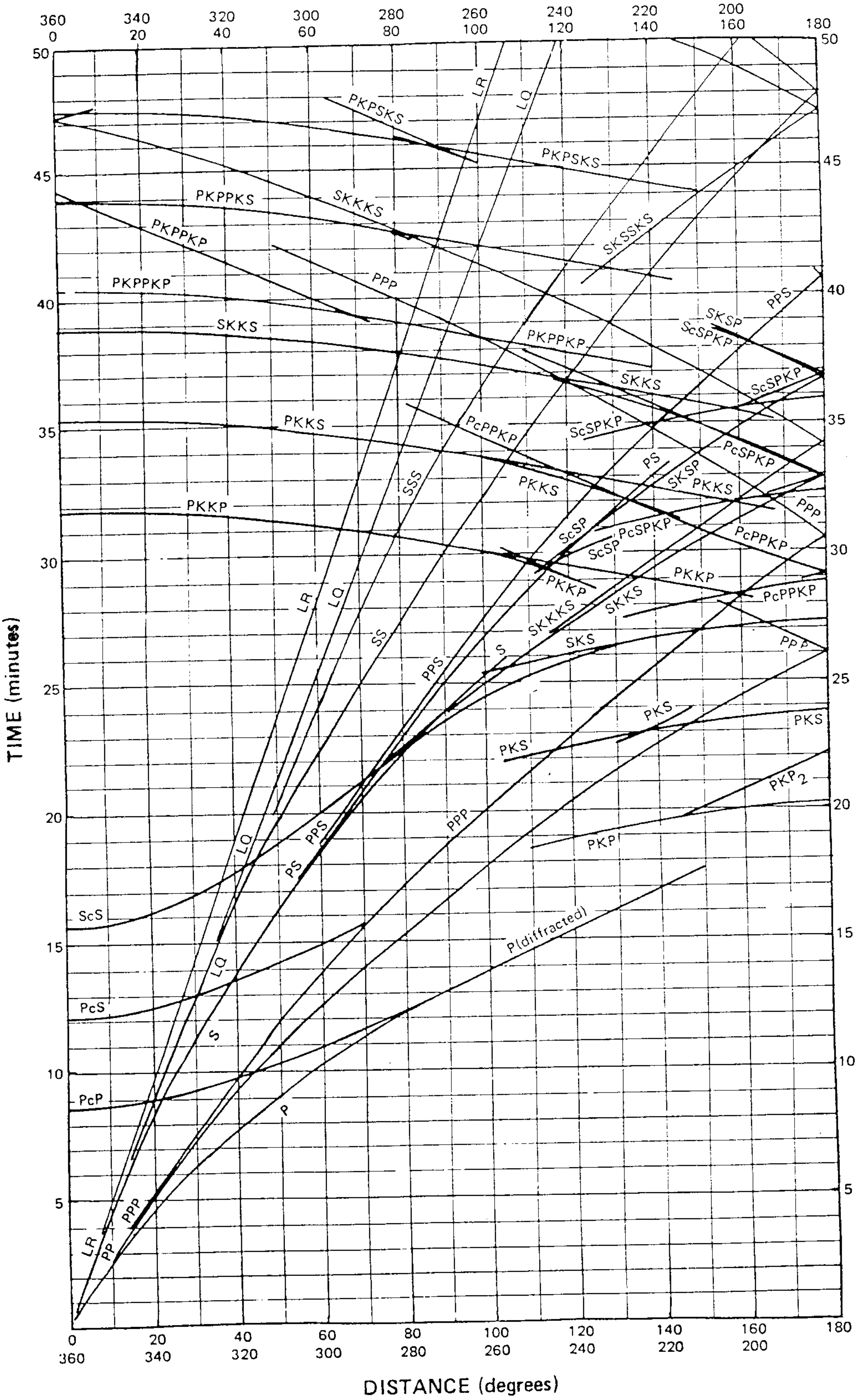

Figure C
Travel-time curves for earthquake phases.

非球対称構造を見る

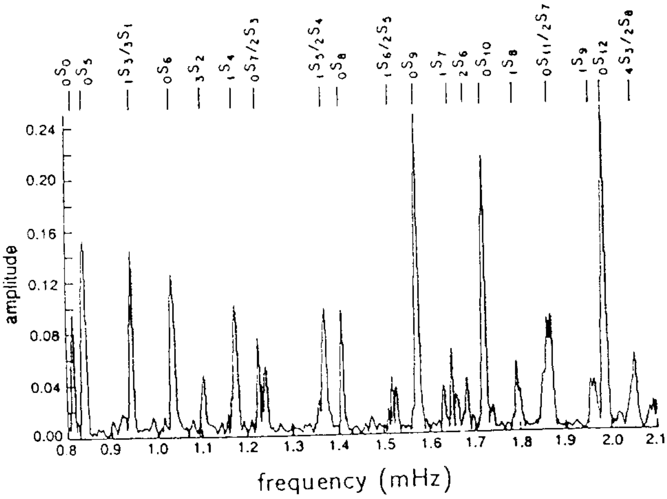

振巾スペ

Fig. 2. Linear amplitude spectra of the RAR record for the 1977 Indonesia earthquake. After RITZWOLLER *et al.* (1988).

↓ 微細構造

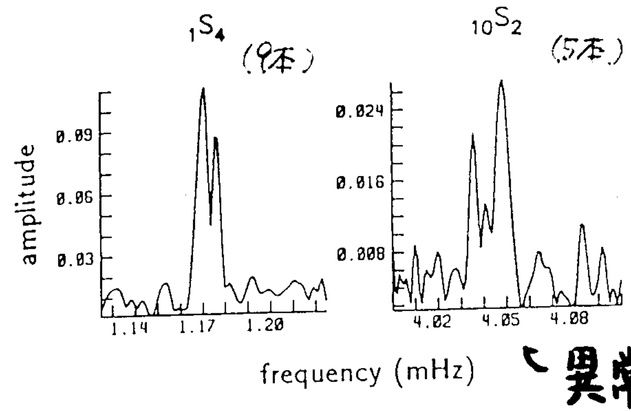

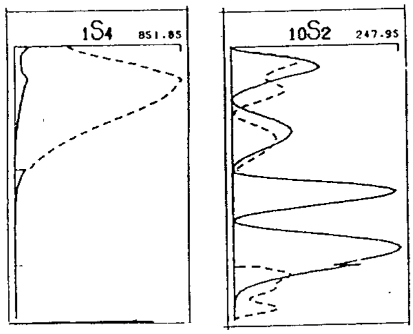

異常分裂

エネルギー分布

Fig. 3. Linear amplitude spectra of the two low degree modes, $_1S_4$ and $_{10}S_2$, which are from the CMO and NNA records for the 1977 Indonesia earthquake, respectively. Splitting of $_{10}S_2$ is about 2.5 times wider than that expected from a rotating earth in hydrostatic equilibrium. After RITZWOLLER *et al.* (1986).

分裂数

$= 2l+1$

非球対称構造がスペクトルに及ぼす影響

$_0S_2$ の splitting

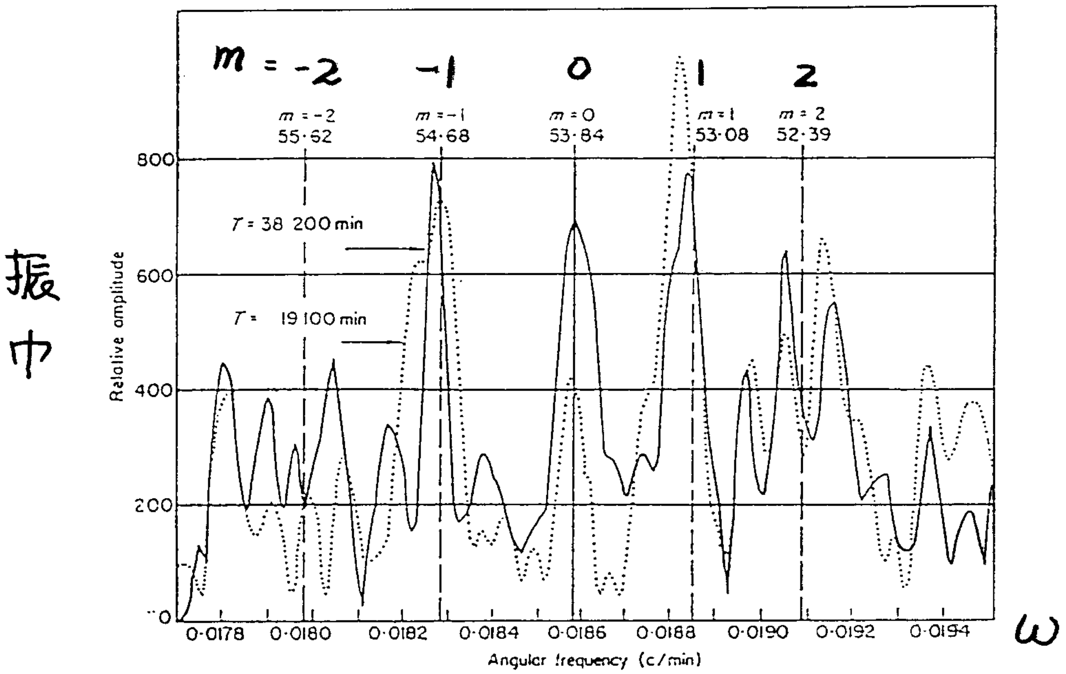

FIG. 2. Fine resolution of poloidal quintet $_0S_2$. Recorded after Chilean earthquake of 1960 on a quartz strain gauge located at Isabella, California. Fourier analysis of two lengths of record, 19 100 min and 38 200 min, sample interval 2 minutes (data from Smith (1961)). The dashed vertical lines represent the computed positions (periods designated in minutes) of the $m = \pm 1$ and $m = \pm 2$ peaks for model 1 (see text).

1960 チリ地震

Dahlen (1968)

l のモード → $2l+1$ に分裂

マルチプレット

自由振動で見た非球対称構造

原因

Ritzwoller et al (1986)

外核のせい X

Woodhouse et al (1986)

内核の異方性

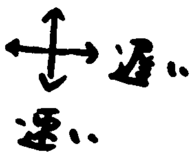

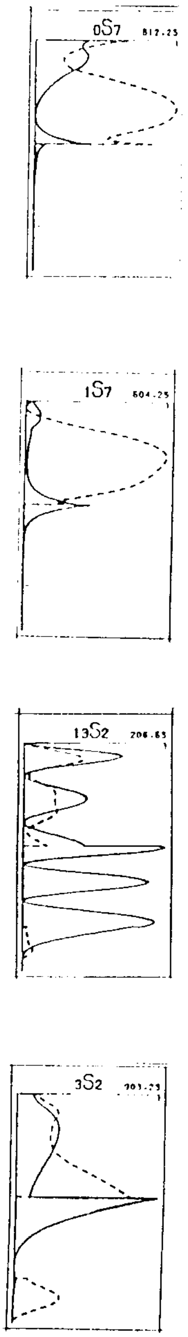

エネルギー分布

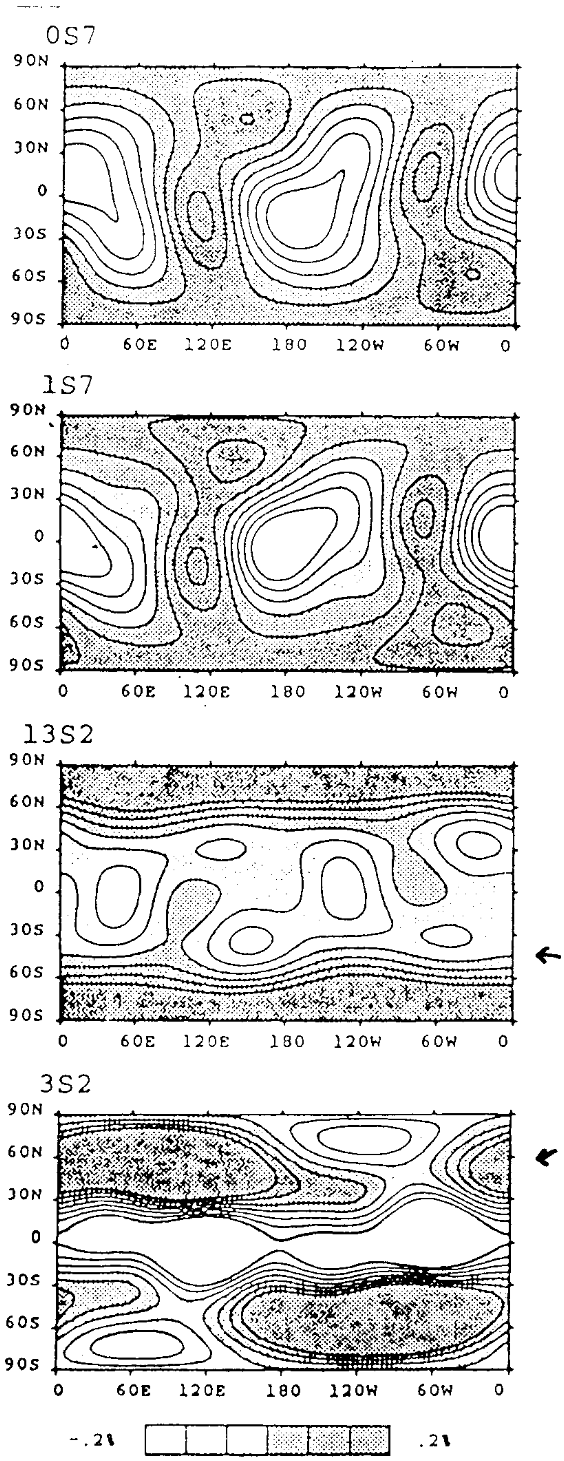
0S7
1S7
13S2
3S2
90N
60N
30N
0
30S
60S
90S
0
60E
120E
180
120W
60W
0
-.21
.21

スプリッティング関数

Core Undertone （慣性重力波）

- 内核 - 外核の密度
- 外核内の密度成層

$$-\omega^2\vec{u} + 2i\omega\vec{\Omega}\times\vec{u} = -\nabla\chi - \vec{g}_0\psi \qquad \left(\chi = \frac{P_1}{\rho_0} - V_1\right.$$

$$\psi = \beta\nabla\cdot\vec{u} = -\frac{\beta}{\alpha^2}\vec{u}\cdot\vec{g} \qquad \left(\beta = -\left(\frac{\alpha}{g_0}N\right)\right.$$

$$\nabla^2 V_1 = 4\pi G\rho_0\psi$$

$$\Downarrow$$

$$\underline{\left\{\sigma^2\nabla^2 - (\hat{k}\cdot\nabla)^2\right\}\chi = \frac{A}{B}\vec{c}\cdot\nabla\chi + \vec{c}^{\,*}\cdot\nabla\left(\frac{\vec{c}\cdot\nabla\chi}{B}\right)}$$

$$\begin{cases} A = \dfrac{\omega^2}{\beta}(\sigma^2-1) + \sigma^2(4\pi G\rho_0 - 2\Omega^2) + (\hat{k}\cdot\nabla)(\hat{k}\cdot \\ B = \dfrac{\alpha^2\omega^2}{\beta}(\sigma^2-1) + \sigma^2 g_0^2 - (\hat{k}\cdot\vec{g}_0)^2 \\ \vec{c} = (\hat{k}\cdot\vec{g}_0)\hat{k} + i\sigma\hat{k}\times\vec{g}_0 - \sigma^2\vec{g}_0 \end{cases}$$

$\beta \to 0$ のとき $\dfrac{\vec{c}\cdot\nabla\chi}{B} \to 0$.

さらに

$\alpha^2 \to \infty$ のとき $\dfrac{A}{B} \to 0$.

N²

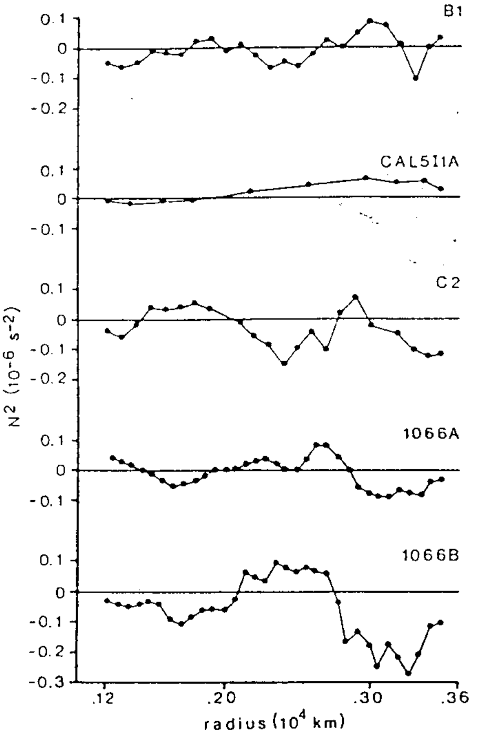

gure 6. Core stability N^2 for several realistic Earth models.

N の上限

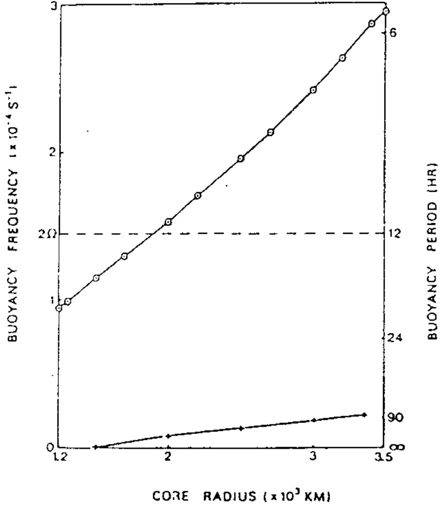

Fig. 1. Buoyancy limits for the liquid core. The seismological upper limit is given by the curve ⊙–⊙ (Masters, 1979) and the lower curve + – + is from the thermal discussion of Gubbins et al. (1982).

↑

↖ 地震学的に求められた
外核の密度成層

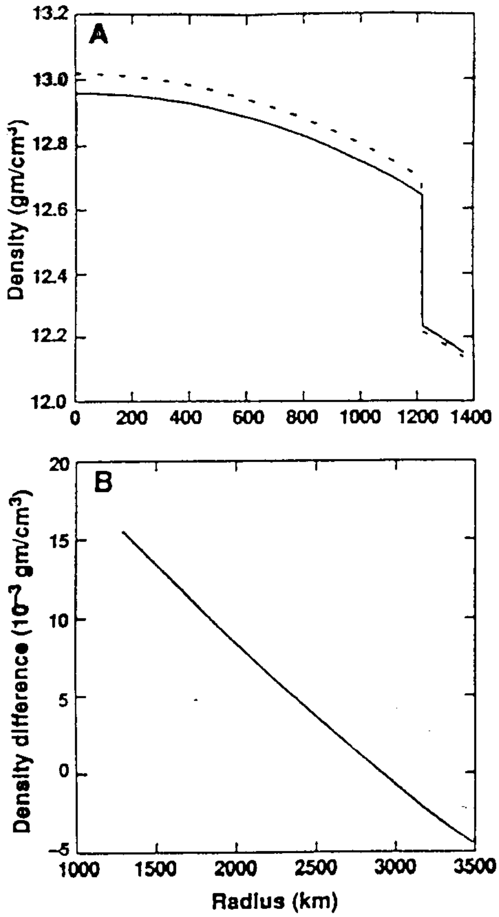

内核の横ずれ振動
(Smylie 1992)

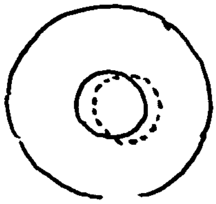

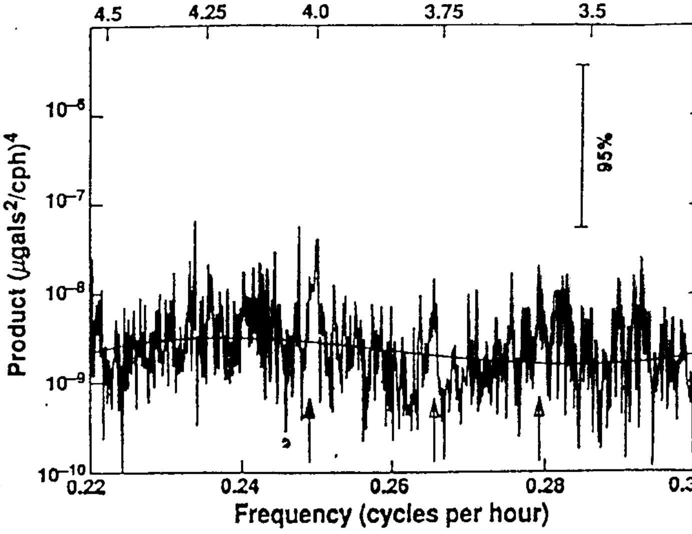

木星の内部構造

モデルの作り方

1 構成物
  a) H, He
  b) ice : H_2O, CH_4, NH_3
  c) rock : SiO_2, MgO, Fe, Ni

2 ぶつり.
  a) 静水圧平衡
  b) 状態方程式
  c) 断熱温度構造

3 合わせるパラメータ
  重さ
  半径
  J_2, J_4

"試行錯誤"

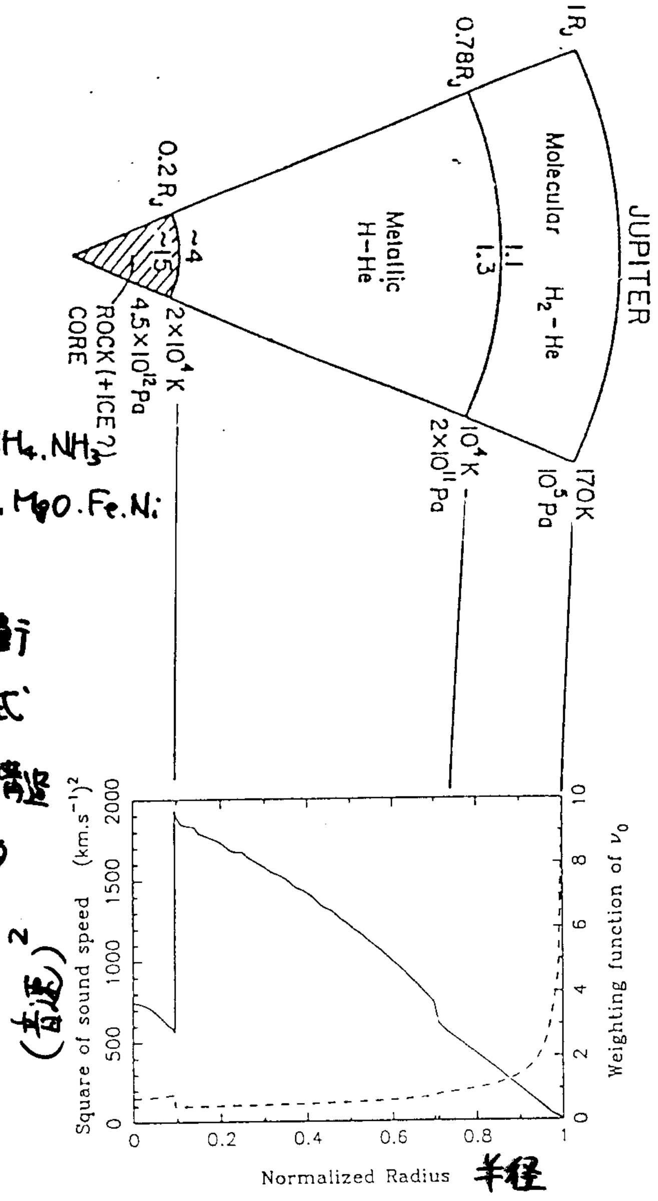

Stevenson (198

Hubbard & Marley (19

Fig. 5. Square of sound speed (full line) and weighting function (dashed line) calculated from Hubbard & Marley (private communication). The weighting function indicates the contribution to v_0 of each $0.01 \times R_J$ thick layer. Because of adiabatic equilibrium throughout the entire planet, the square of sound speed is simply derived from $\Delta p/\Delta \rho$. The first discontinuity ($\sim R_J/10$) corresponds to the core, the second is an artefact due to the interpolated equation of state between the metallic and molecular hydrogen regions: it may explain the too high theoretical value of v_0, because of an overestimated sound speed in the metallic region

木震の観測

TABLE IV
Jovian Seismology Observation Techniques

principle	resonance spectroscopy (1 line)	Fourier spectroscopy (≡5 lines)	photometry	heterodyne spectroscopy (1 line)
observatory	OHP	CFH	IRTF	IRTF
publication	Schmider *et al.* 1991	Mosser *et al.* 1992b	Deming *et al.* 1989	Mosser *et al.* 1992a
positive result	yes	yes	no	
reference	local line	laser	×	laser
spectrum	solar	solar	Jovian	Jovian
line	Na, D2	CH_4, $3\nu_3$	×	H_2, S(1)
λ *(*μm*)*	0.58	1.1	8→13	17.2
field	full disk	circular diaphragm	linear diaphragm	circular diaphragm
degree	0→3	1→8	5→50	0→30
selection rule $(\ell + m)$	even	odd	$\|m\| = \ell$	×
pointing errors	no	.... must be corrected		
$1\,m.s^{-1}$ *level (hour)*	8	8	24	12
observation period	opposition strictly	.... opposition		
advantage	– well known technique – full disk	– calibration – performance		– observation near the tropopause
disadvantage	– 4 m tel. – opposition	4 m tel.	– 4 m tel. – selection	new technique

Mosser 1993
et al.

パワースペクトル

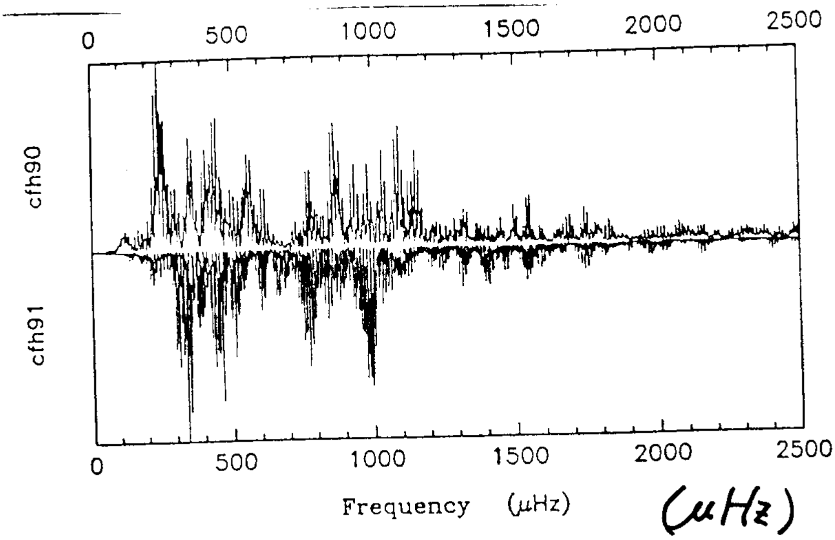

(μHz)

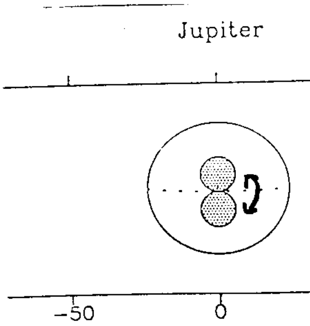

Autocorrelation of the spectrum cfh91

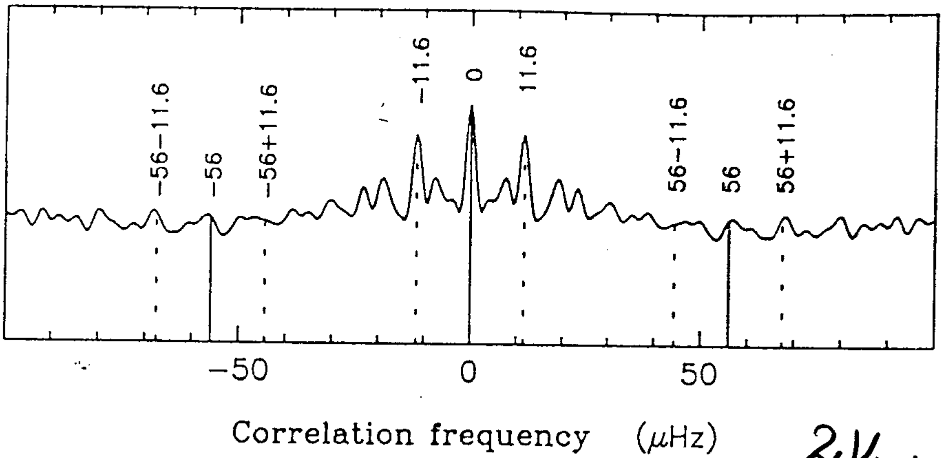

$2\nu_{rot} = 56$

Spectrum of the spectrum cfh91

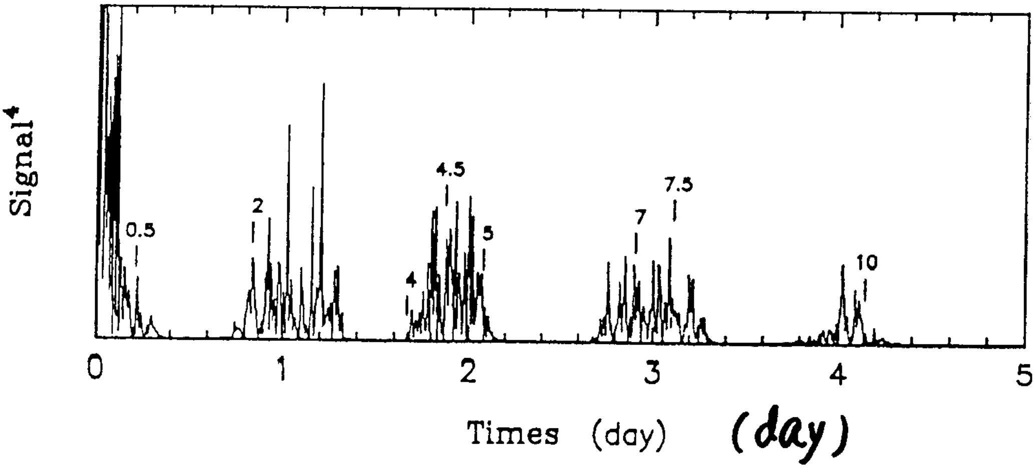

(day)

観測パワースペクトル

昼は見えな

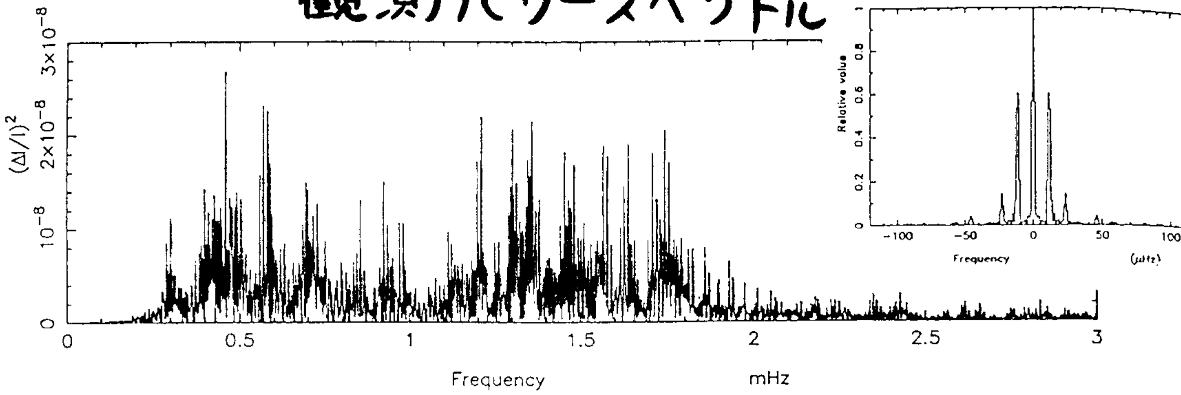

Fig. 2a. Power spectrum of the monochromatic signal obtained on Jupiter, observed during 5 nights at Haute-Provence Observatory in square of the relati
intensity. The corresponding amplitude in radial velocity is about 8 m s^{-1} for the most important peaks. In the upper corner, the window function due to the da
interruption in the data is shown

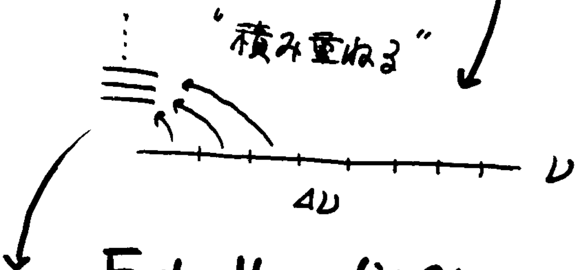

Echelle-diagram

mHz

周波数

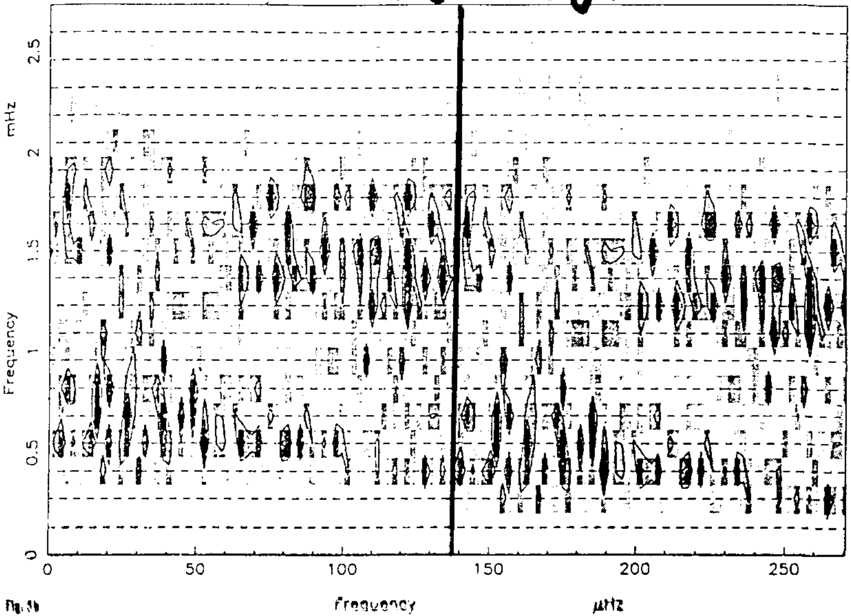

Fig. 3b

Δ 周波数 μHz

パワースペ
のコンター

Δν=13

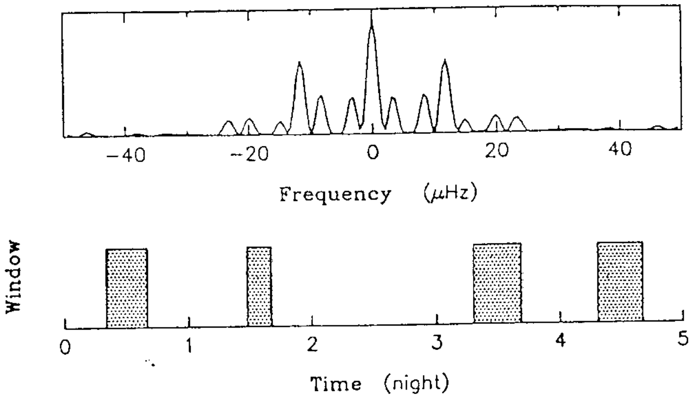

Fig. 13. The window function of 1991. The daily interruption of observations – the window effect – adds secondary peaks at 11.6 μHz [$= (1\,\mathrm{d})^{-1}$], while the interruption due to bad weather on the third day adds tertiary peaks at 3.85 μHz [$= (3\,\mathrm{d})^{-1}$]

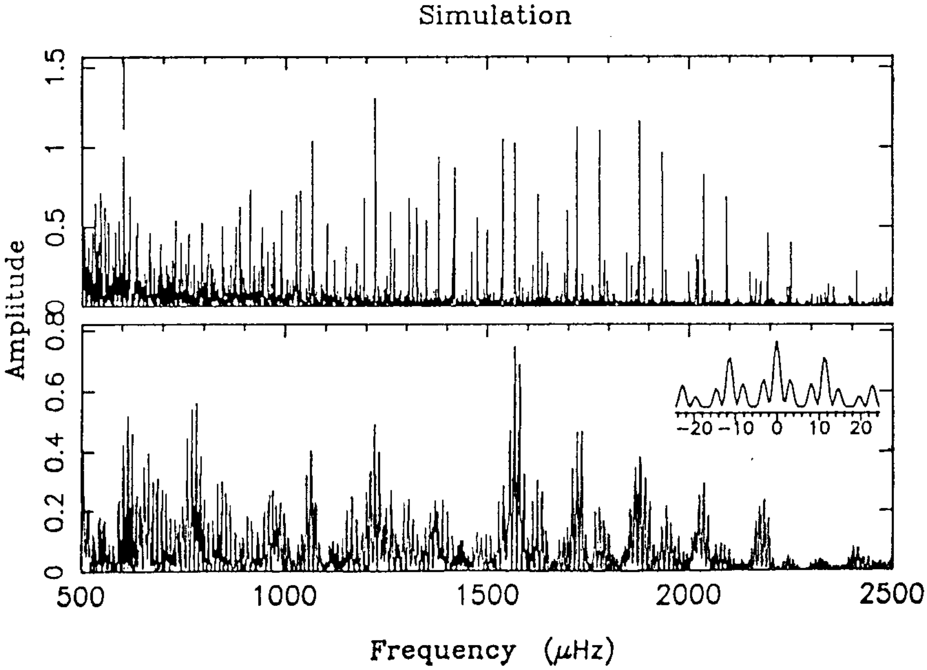

モードの同定

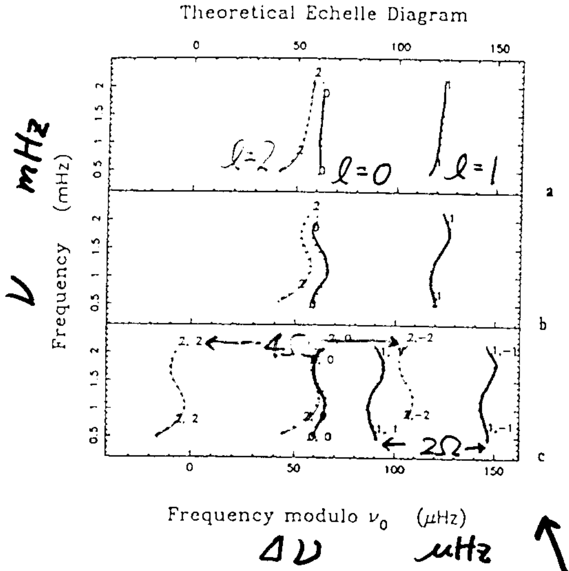
Theoretical Echelle Diagram

非回転・連続モデル

$$\nu_{n\ell} \simeq \left(n + \frac{\ell}{2} + \varepsilon\right)\nu_0$$

非回転・不連続モデル

$$\nu_{n0} \cong \left(n + \varepsilon + \underline{\varepsilon' \sin\frac{n}{N}}\right)\nu_0$$

回転・不連続モデル

$$\nu_{n\ell m} = \nu_{n\ell} - \underline{m\Omega}$$

探し方

echelle diagram 上で c のような構造をさがす.

$\nu_0 = 125-145\ \mu Hz$

< モデルの ν_0

$\simeq 160\ \mu Hz$

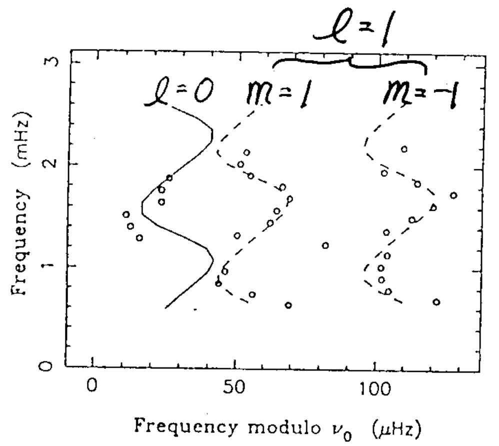

Fig. 3. Identification of the $l = 0$ and $l = 1$ p-modes in the échelle diagram representation. Circles correspond to the most significant observed peaks, and lines to the theoretical pattern (full line: $l = m = 0$, dashed line: $l = 1, m = \pm 1$). For $l = 1$ modes, we have retained among the multiple lines due to the window function, those which contribute the best to the rotational splitting

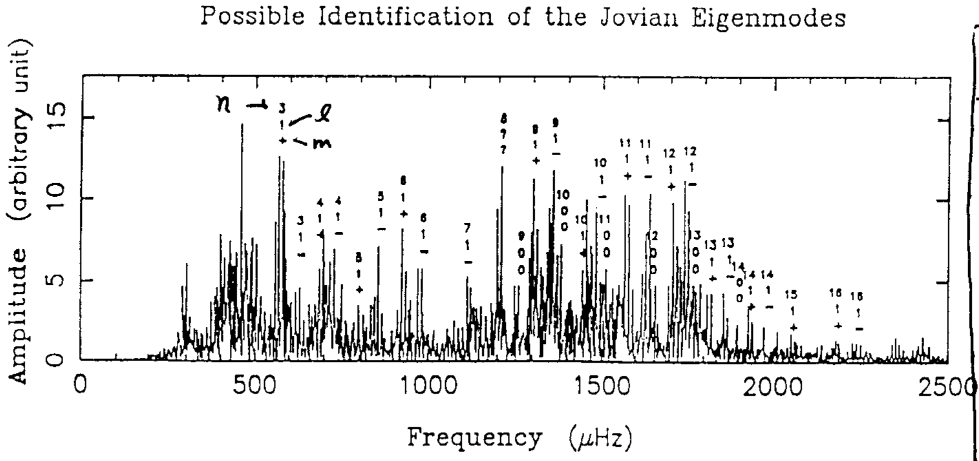
Possible Identification of the Jovian Eigenmodes

Fig. 4. Identification of the $l = 0$ and $l = 1$ p-modes in the observed Fourier spectrum. The values of the radial order n, the degree l and the azimuthal order m ($\pm$ signifies $m = \pm 1$) are given for each identified eigenmode

同定された

ℓ=0	ℓ
n=9	[illegible]
10	4
11	5
12	6
13	7
14	9
	10
	11
	12
	13

木星

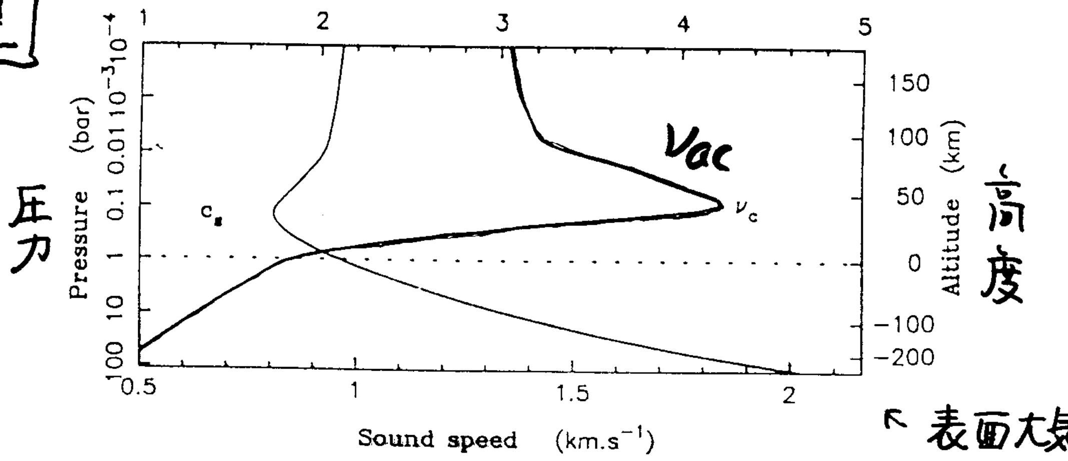

Fig. 23. The acoustic cutoff frequency and the sound speed in the troposphere and low stratosphere. Zero altitude corresponds to the 1-bar pressure level. Modes with lower frequency than 3 mHz are trapped; modes with frequency in the range from 3 to 4 mHz are only partially trapped

propagation cavity

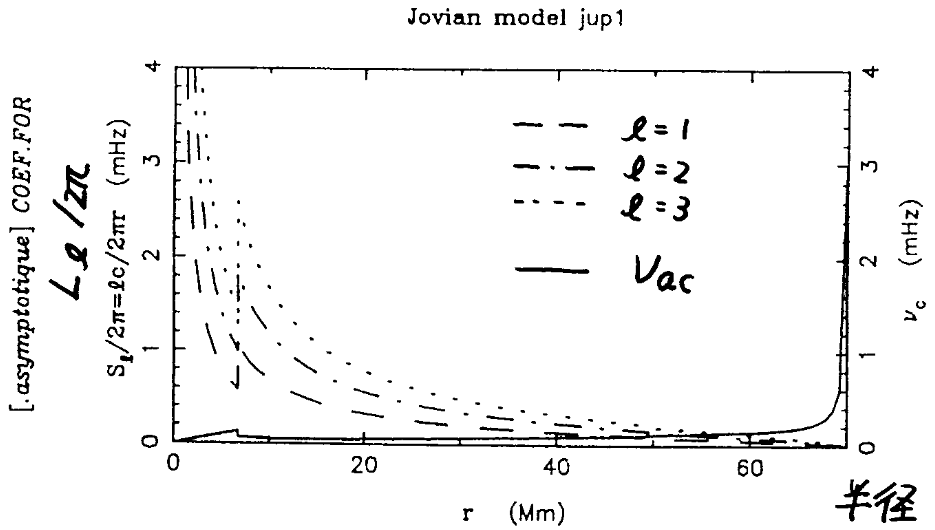
Jovian model jup1

Fig. 24. Pressure modes propagate in the cavity determined by the Lamb frequency ($\nu_c = \omega_c/2\pi$), i.e. in the region where the eigenfrequency exceeds $S_\ell/2\pi$ and ν_c. Therefore, the inner boundary depends on the degree ℓ: radial modes ($\ell = 0$) propagate through the core, whereas non-radial modes test different regions of the planet. Full line: ν_c, dashed, dot-dashed and doted lines: $S_\ell/2\pi$ for $\ell = 1$, 3 and 5: respectively.

TABLE III
Frequencies

Planet	ν_p	ν_0^*	ν_{rot}	ν_c^{**}
	....	(μHz)	....	(mHz)
Jupiter	94	155	28	3.0
Saturn	66	100	26	1.6
Uranus	100	170	16	1.8
Neptune	104	190	18	2.2

ν_p : $\sqrt{GM/R^3}/2\pi$
ν_0 : characteristic frequency of the oscillations
ν_{rot} : rotation

MOSSE
1993